Second Harmonic-Induced Ultrafast Wrinkle Formation in Two-Dimensional Material

Xiaodong Wang[1†], Yongzhao Zhang[2†*], Shuaishuai Sun[3,4], Jun Li[3,4], Shaobo Cheng[1,2*], and Huaixin Yang[3,4*]

[1]*Henan Key Laboratory of Diamond Optoelectronic Materials and Devices, Key Laboratory of Material Physics, Ministry of Education, School of Physics and Laboratory of Zhongyuan Light, Zhengzhou University, Zhengzhou 450052, China*

[2]*Institute of Quantum Materials and Physics, Henan Academy of Sciences, Zhengzhou 450046, China*

[3]*Beijing National Laboratory for Condensed Matter Physics and Institute of Physics, Chinese Academy of Sciences, Beijing 100190, China*

[4]*School of Physical Sciences, University of Chinese Academy of Sciences, Beijing 100190, China*

(Received 9 March 2025; accepted manuscript online 24 March 2025)

The precise control of wrinkles and strain gradients in nanofilm is of significant interest due to their profound influence on electronic band structures and spin states. Here, we employ ultrafast electron diffraction (UED) to study the picosecond-scale dynamics of laser-induced bending in 2H-$MoTe_2$ thin films. Owing to the sample thickness exceeding the laser penetration depth, inhomogeneous excitation leads to the emergence of both fundamental (21 GHz) and second harmonic (42 GHz) acoustic phonons. The experimental and simulation results demonstrate that the second harmonic directly generates a strain gradient along the *c*-axis, which subsequently transforms into in-plane strain through the Poisson effect. This nonuniform in-plane strain serves as the primary driving force for film bending. This study not only demonstrates ultrafast laser-based control of internal strain gradients but also provides new insights into the mechanisms of laser-induced bending mediated by coherent phonons, particularly the second harmonic.

DOI: 10.1088/0256-307X/42/4/047201 CSTR: 32039.14.0256-307X.42.4.047201

1. Introduction. In materials engineering, wrinkle-induced strain gradients have emerged as critical design parameters for advanced functional materials, particularly in flexoelectric and flexomagnetic systems.[1,2] The inherent asymmetry of wrinkles in thin-film architectures creates distinct nonuniform strain distributions between upper and lower surfaces. Such strain gradients fundamentally disrupt local inversion symmetry within the crystal lattice, thereby enabling the emergence of novel electronic states through symmetry-controlled mechanisms.[3–7] For instance, in graphene, such nonuniform strain can quantize electron orbitals into Landau levels, creating flat bands and localized electron states.[8] Similarly, in Heusler alloy films, strain states near wrinkles can drive an antiferromagnet to ferri- or ferromagnetic transition.[9] This ability to modify physical properties through wrinkle engineering highlights its potential as a versatile tool for designing advanced functional materials. Consequently, understanding and harnessing the effects of wrinkles and associated strain gradients represents a frontier in materials science, offering new pathways to tailor material responses for technological applications.

Recent advancements[10,11] in ultrafast strong excitations have introduced innovative approaches for manipulating physical properties, such as through strain or Floquet engineering.[12,13] Particularly, inhomogeneous excitation opens new possibilities for ultrafast material control through the introduction of strain gradients,[14] such as the novel electronic state triggered by nonuniform ultrafast laser excitation in a charge density wave (CDW) system.[15] The dynamics of wrinkle formation in thin films under homogeneous excitation can be regulated by coherent acoustic phonons, accompanied by ultrafast delamination of the film.[16] However, the effects of inhomogeneous excitation on wrinkles remain poorly understood, lacking both experimental observations and mechanistic explanations.

In contrast to homogeneous excitation regimes,[17,18] inhomogeneous optical driving generates higher-order harmonic coherent acoustic phonons,[19,20] which mediate the transition from standing waves to directional propagating waves along the surface normal.[21] Using ultrafast electron diffraction with femtosecond temporal resolution, we directly resolve the laser-induced wrinkle formation dynamics in 2H-$MoTe_2$ thin films. Our measurements reveal synchronized oscillations between wrinkle evolution and dynamic lattice reorientation, exhibiting identical frequency characteristics to the coherent acoustic phonons. Through the simulations of acoustic waves, we elucidate the second harmonic-induced driving force for the film bending,

†These authors contributed equally to this work.
*Corresponding author. Email: hxyang@iphy.ac.cn; zhangyz@hnas.ac.cn; chengshaobo@zzu.edu.cn
© 2025 Chinese Physical Society and IOP Publishing Ltd. All rights, including for text and data mining, AI training, and similar technologies, are reserved.

providing a new perspective for understanding wrinkle formation on the picosecond timescale under inhomogeneous excitation in nanofilm.

2. Methods. All ultrafast measurements were carried out at room temperature (300 K) with a laser repetition rate of 33 kHz. The pump laser has a wavelength of 515 nm and a pulse width of 300 fs. The fluence of the pump laser used is 4.4 mJ/cm^2 with spot size of 50×60 μm (FWHM). The angle of incidence of the pump laser relative to the horizontal plane is 22.7°. More details about the ultrafast transmission electron microscope (UTEM) based on the pump-probe technique can refer to our previous report.[21]

A multilayer 2H-$MoTe_2$ film was obtained through mechanical exfoliation from a bulk crystal and subsequently transferred onto a carbon nanotube substrate. 2H-$MoTe_2$ possesses a hexagonal structure with space group P_{6_3}/mmc and a honeycomb-like in-plane structure.[22] The sample thickness is 63 nm which has been confirmed by electron energy loss spectroscopy (EELS) measurements.[21]

3. Results and Discussion. The experimental schematic is presented in Fig. 1(a). To obtain out-of-plane information, the sample is tilted by 26.8° around the [100] axis, positioning the incident photoelectron beam parallel to the [021] zone axis of the crystal. In this arrangement, the angle between the pump laser (515 nm) and the sample surface is 50.5°. Figure 1(b) shows the diffraction pattern of 2H-$MoTe_2$ produced by photoelectrons at a negative time delay. After laser excitation, out-of-plane spots [(hkl) with $l \neq 0$] display intensity oscillations, as shown in Fig. 1(c). The corresponding Fast Fourier Transform (FFT) spectrum presented in Fig. 1(d) reveals the excitation of two distinct oscillation modes, exhibiting a frequency ratio of 1 : 2. To fit the intensity, we employ a combination of sinusoidal functions with periods of T_I and $T_I/2$.

$$\frac{I}{I_0} = \sum_{k=1}^{2} A_{Ik} \sin\left(\frac{2\pi k}{T_I} t + \varphi_{Ik}\right), \tag{1}$$

where A_I, T_I and φ_{Ik} represent the amplitude, period and phase of the intensity oscillation, respectively. The well-fitted results are depicted as blue curves in Fig. 1(c), which yield a vibration period (T_I) of 47.6 ± 0.5 ps [for $(\bar{1}2\bar{4})$ peak] and the corresponding frequency of 21 GHz. Additional fitting results can be found in Section S1 of the Supplementary Information. These oscillations indicate the out-of-plane breathing mode driven by thermoelasticity[23] and deformation potential (electric stress),[24,25] which has been confirmed in our previous report.[21] For 2H-$MoTe_2$ films exceeding the critical thickness of 40 nm,[21] inhomogeneous excitation induces depth-dependent lattice expansion along the c-axis. This strain gradient disrupts the coherence of electrons scattered by planes with Miller indices (hkl) where $l \neq 0$, resulting in damped diffraction intensity. The presence of fundamental and second harmonic components under inhomogeneous excitation is schematically illustrated in Fig. 1(e).

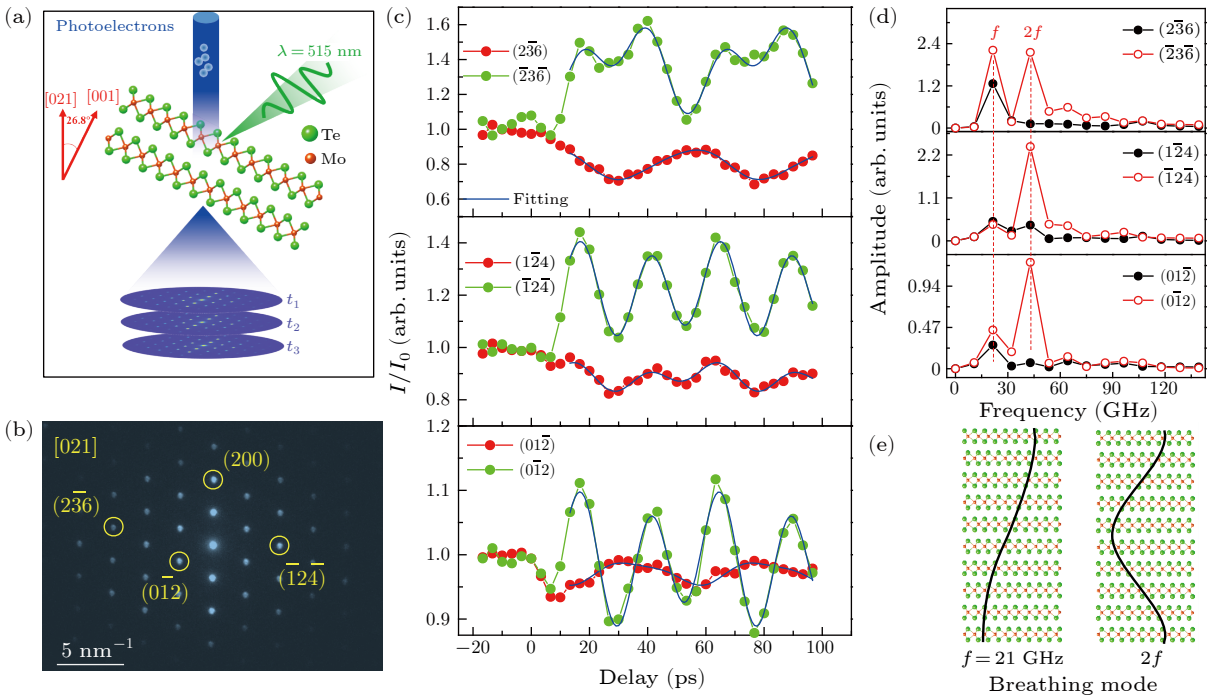

Fig. 1. Temporal evolution of diffraction intensity in the 63 nm 2H-$MoTe_2$ thin film. (a) Experimental configuration with the sample tilted to capture out-of-plane dynamics. (b) Diffraction pattern along the [021] zone axis. (c) Intensity oscillations of several Bragg peaks. The blue lines represent fitting curves using $\frac{I}{I_0} = \sum_{k=1}^{2} A_{Ik} \sin(\frac{2\pi k}{T_I} t + \varphi_{Ik})$. $T_{I\ (\bar{1}2\bar{4})} = 47.6 \pm 0.5$ ps. Further details regarding the fitting parameters are provided in Section S1. (d) The Fast Fourier Transform (FFT) analysis revealing the excitation of two oscillation modes with a frequency ratio of 1 : 2 (21 and 42 GHz). (e) Schematic of the fundamental and second harmonic under inhomogeneous excitation.

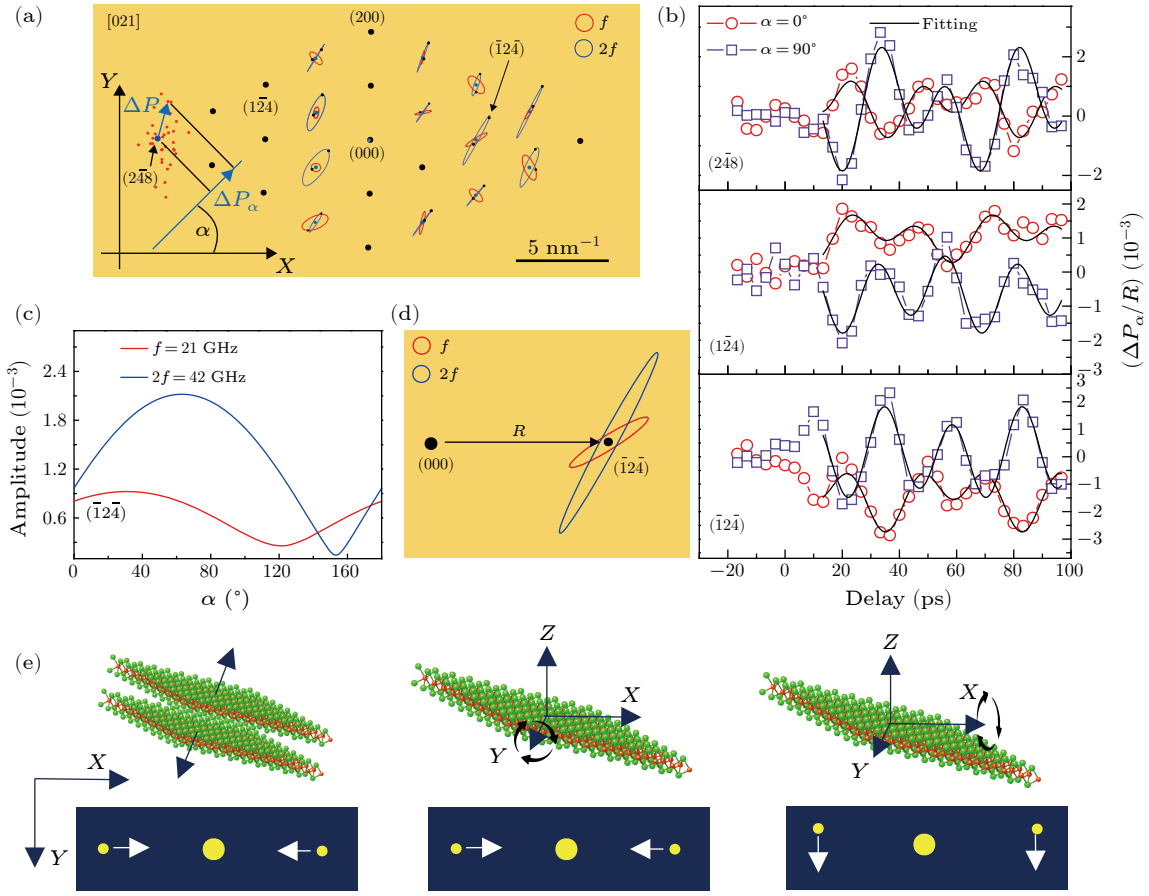

Fig. 2. Temporal evolution of Bragg peak positions in 2H-$MoTe_2$ thin film. (a) The positions of Bragg peaks (red dots) are shown within a time range of −20 ps to 96 ps. The displacements ΔP of these spots are projected onto a direction at an angle α relative to the X-axis (ΔP_α). The red and blue ellipses in the figure represent the trajectories of the Bragg peaks at vibration frequencies of 21 GHz and 42 GHz, respectively. The black dots on the trajectories indicate the oscillation states at 12 ps. (b) Time-dependent displacements of the Bragg peaks (2$\bar{4}$8), (1$\bar{2}$4), and ($\bar{1}$2$\bar{4}$). The black curves revealing the fitting results by $\frac{\Delta P_\alpha}{R} = \sum_{k=1}^{2} A_{pk} \sin(\frac{2\pi k}{T_p} + \varphi_{pk})$, revealing two oscillation periods: 23.9 ps and 47.8 ps ($T_{p,\,\bar{1}2\bar{4}} = 47.8 \pm 1.5$ ps). Further details regarding the fitting parameters are provided in Section S1. (c) The angular dependence of the amplitudes for the fundamental and second harmonic. (d) The elliptical trajectories of ($\bar{1}$2$\bar{4}$) peak after laser excitation. (e) Schematic of the diffraction spot displacement.

After laser excitation, periodic oscillations can also be found in the peak position. As illustrated in Fig. 2(a), the red dots denote the positions of (2$\bar{4}$8) spot within −20 to 96 ps. To enhance visibility, the displacements ΔP have been magnified by a factor of 100 in Fig. 1(a). To analyze this two-dimensional characteristic, we projected the displacements ΔP onto a direction at an angle α relative to the X-axis (denoted as ΔP_α). Figure 2(b) visualizes the periodic oscillation of $\Delta P_\alpha/R$ at $\alpha = 0°$ and $\alpha = 90°$, which is fitted by the same function $\frac{\Delta P_\alpha}{R} = \sum_{k=1}^{2} A_{pk} \sin(\frac{2\pi k}{T_p} + \varphi_{pk})$ as that in intensity oscillation. R represents the reciprocal distance between (hkl) and (000). The fitting result $T_{p(\bar{1}2\bar{4}),\ \alpha=0°} = 47.8 \pm 1.5$ ps indicates two oscillation periods with 23.9 ps and 47.8 ps (almost the same as those in intensity oscillation), corresponding to frequencies of 42 GHz ($2f$) and 21 GHz (f), respectively. Further details regarding the fitting parameters are provided in Section S1. The amplitudes A_{pk} of the fundamental and second harmonic varied with the projection angle α [Fig. 2(c)]. For instance, the amplitude of fundamental in the spot ($\bar{1}$2$\bar{4}$) peaked at $\alpha = 30°$, while that of the second harmonic is maximal at $\alpha = 65°$. The variation in amplitude across different angles indicates that the diffraction spots move along elliptical trajectories in reciprocal space. The elliptical trajectories of partial diffraction spots, exhibiting distinct oscillation signals induced by both fundamental and second harmonic components, are presented in Fig. 2(a), with the ($\bar{1}$2$\bar{4}$) peak specifically highlighted in Fig. 2(d). These trajectories can be understood as the superposition of displacements along the X- and Y-directions. Similar experimental phenomena can be observed in the work of Flannigan *et al.*,[26] where the displacements of diffraction spots were projected in polar coordinates, revealing oscillations in both the axial and radial directions. However, they did not extensively discuss the underlying physical implications.

According to kinematical theory of electron diffraction,[27,28] the position of a diffraction spot is determined by the intersection point of the reciprocal rod with the Ewald sphere. Changes in interplanar spac-

ing and lattice tilt can alter this intersection, leading to displacement of the diffraction spot, as illustrated in Fig. 2(e). Taking the $(2\bar{4}8)$ and $(\bar{1}2\bar{4})$ diffraction spots as examples, their displacements along the X-direction are influenced by both interplanar spacing and sample orientation, making it challenging to deduce the sample state solely from X-direction displacements. Fortunately, displacements along the Y-direction are solely affected by orientation. Thus, by extracting Y-direction displacements, information about sample tilt can be obtained, effectively avoiding the influence of lattice expansion. The black solid line in Fig. 2(b) represents the sinusoidal fitting results. Through these fitting procedures, the two distinct oscillation modes of the $(2\bar{4}8)$ and $(\bar{1}2\bar{4})$ diffraction spots along the Y-direction are successfully extracted and presented in Fig. 3(e). Figure 3(a) visually demonstrates the displacements ($\alpha = 90°$) induced by the second harmonic frequency at 33 ps and 68 ps. Notably, the displacement vibrations of the Friedel pairs are nearly in-phase, indicating the sample tilt around the X-axis. In reality, it is unlikely for the sample to exhibit uniform tilt under laser irradiation. A more plausible scenario is that the sample undergoes bending. To validate this, we measured the full width at half maximum (FWHM) of the diffraction spots, as shown in Fig. 3(b), which are well-fitted by sinusoidal functions $\frac{\Delta r}{r_0} = \sum_{k=1}^{2} A_{rk} \sin(\frac{2\pi k}{T_r} + \varphi_{rk})$ with $T_{r,(\bar{1}2\bar{4})} = 48.5 \pm 1.2$ ps and $T_{r,(2\bar{4}8)} = 48.3 \pm 0.7$ ps. The FWHM exhibits two oscillation modes with frequencies of 21 GHz and 42 GHz [Fig. 3(c)]. Figure 3(d) provides a schematic illustration of the FWHM changes of $(2\bar{4}8)$ and $(\bar{1}2\bar{4})$ spots. The bending of the film induces splitting of the reciprocal lattice rod, creating multiple intersection points with the Ewald sphere. This phenomenon manifests as spot broadening and an increased full width at half maximum (FWHM). The oscillatory profiles fitted in Fig. 3(b) were systematically analyzed and compared with the positional oscillations presented in Fig. 3(e). Remarkably, all oscillatory curves demonstrate nearly identical phase relationships. Specifically, the analysis of curves A and B reveals a direct correlation between the maximum FWHM of the diffraction spots and the maximum tilt angle of the thin film. These experimental observations provide conclusive evidence that film bending is the primary mechanism responsible for film tilting.

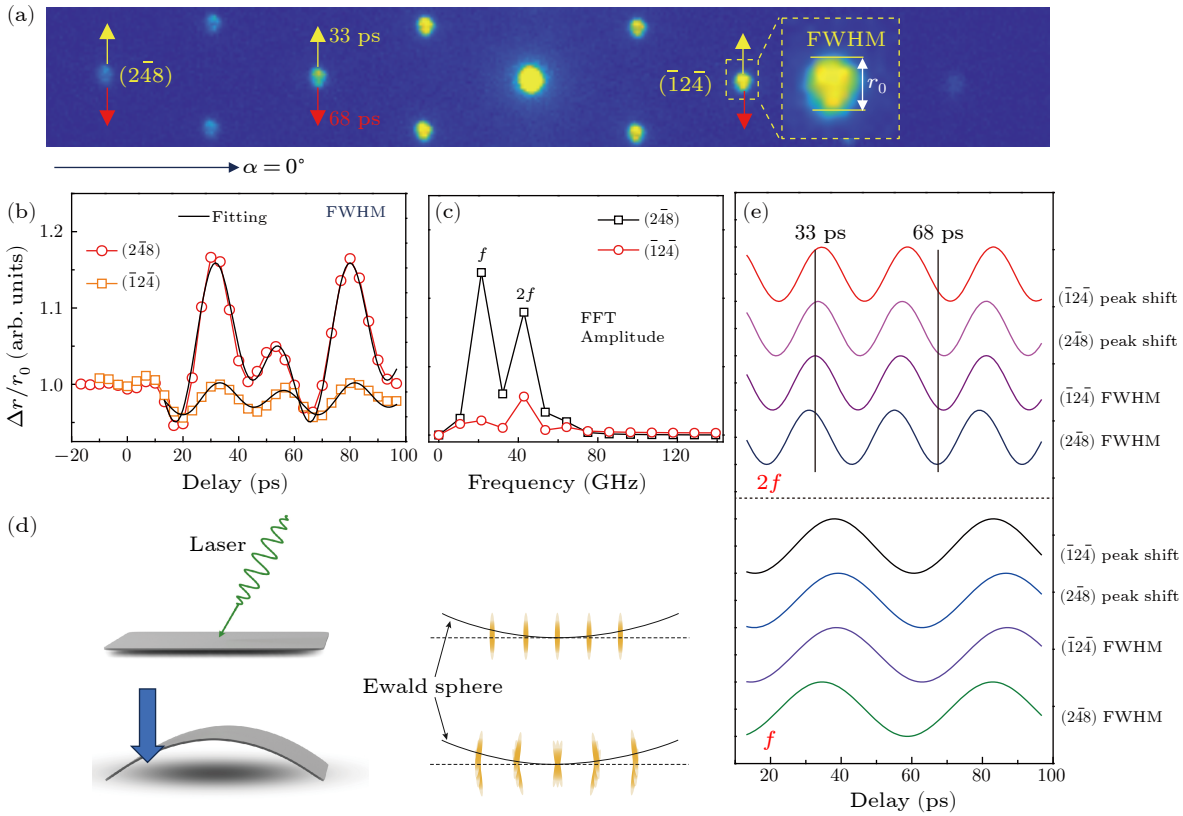

Fig. 3. Analysis of sample bending and its effects on diffraction spot broadening. (a) Displacements ($\alpha = 90°$) induced by the second harmonic at 33 ps and 68 ps. The in-phase oscillation of Friedel pairs indicates the sample tilt around the X-axis ($\alpha = 0°$). (b) Measurement of the full width at half maximum (FWHM) of the diffraction spots. The oscillatory curves are well-fitted by sinusoidal function $\frac{\Delta r}{r_0} = \sum_{k=1}^{2} A_{rk} \sin(\frac{2\pi k}{T_r} + \varphi_{rk})$, with oscillation period $T_{r,(\bar{1}2\bar{4})} = 48.5 \pm 1.2$ ps and $T_{r,(2\bar{4}8)} = 48.3 \pm 0.7$ ps. (c) FFT of (b). FWHM oscillations show frequencies of 21 GHz and 42 GHz. (d) Schematic illustrating how sample bending induces splitting of the reciprocal lattice rod and its intersection with the Ewald sphere, leading to diffraction spot broadening. (e) Comparison of the oscillations in FWHM and peak positions. All these curves are extracted from experimental results by sinusoidal fitting. The amplitudes of the curves can be found in supplementary Tables S2 and S3.

To clarify the driving force for the film bending, we calculate the layer motion μ along the z direction triggered by coherent phonons under laser irradiation. The thickness of the film used in the simulation is 63 nm, and the laser wavelength is 512 nm, as shown in Fig. 4(a). The 2H-$MoTe_2$ film is regarded as a one-dimensional continuous elastic medium, and its wave equation can be depicted as follows:

$$\rho\frac{\partial^2\mu}{\partial t^2} = C_{ij}\frac{\partial^2\mu}{\partial z^2} + \lambda\frac{\partial\mu}{\partial t} + \frac{\partial\sigma_{\text{ext}}}{\partial z}, \tag{2}$$

where C_{ij}, λ, and ρ represent the components of elastic modulus matrix, damping constant, and density, respectively. In the calculation of the longitudinal wave, C_{ij} is equal to C_{33} which represents the out-of-plane Young's modulus.[29] The depth z is along the normal direction of the surface. σ_{ext} is the photo-induced stress term that is mainly composed of thermoelasticity σ_T and deformation potential σ_e. In general,

$$\begin{aligned}
&\sigma_{\text{ext}} = \sigma_T(z,\,t) + \sigma_T(z,\,t),\\
&\sigma_T(z,\,t) = -C_{ij}\beta[T(z,\,t) - T(z,\,0)],\\
&\sigma_e(z,\,t) = -d_e n(z,\,t),
\end{aligned} \tag{3}$$

where β and d_e represent the linear expansion coefficient and deformation potential, respectively. The lattice temperature $T\,(z,\,t)$ and carrier density $n\,(z,\,t)$ are functions of depth z and time delay t. More details regarding the simulation can be found in the Supplementary Information.

Dynamic simulation of depth-dependent atomic displacements is shown in Fig. 4(b). In the case of the 63 nm thickness, the sample is inhomogeneously excited, leading to a traveling wave propagating along the surface normal. Figure 4(c) plots the atomic displacements in the top and bottom layers. Under inhomogeneous excitation, these displacements exhibit asymmetry at different time delays. The brown curve in Fig. 4(c) represents the summation of displacements between the upper and lower layers, clearly showing oscillations with a period of about 24 ps (synchronized with the $2f$ oscillation). This displacement asymmetry directly reflects the difference in the expansion rates between the upper and lower layers of the thin film. For materials with a positive Poisson's ratio, expansion along the c-axis induces contraction in the a–b plane. The disparity in the expansion rates between the upper and lower layers leads to different in-plane compressive stresses at the top and bottom surfaces, ultimately causing film bending, as illustrated in Fig. 4(d). In contrast, the lattice expansion induced by the fundamental mode maintains inversion symmetry throughout the film, which theoretically eliminates the possibility of wrinkle formation. However, real materials often contain numerous lattice defects or pre-existing strain.[30] These defects can lead to the emergence of nonlinear phenomena[31] even under homogeneous excitation. Higher harmonic phonons intrinsically possess the capability to couple with in-plane strain, providing a pathway for the conversion of out-of-plane phonons to in-plane phonons and shear strain.[32–34]

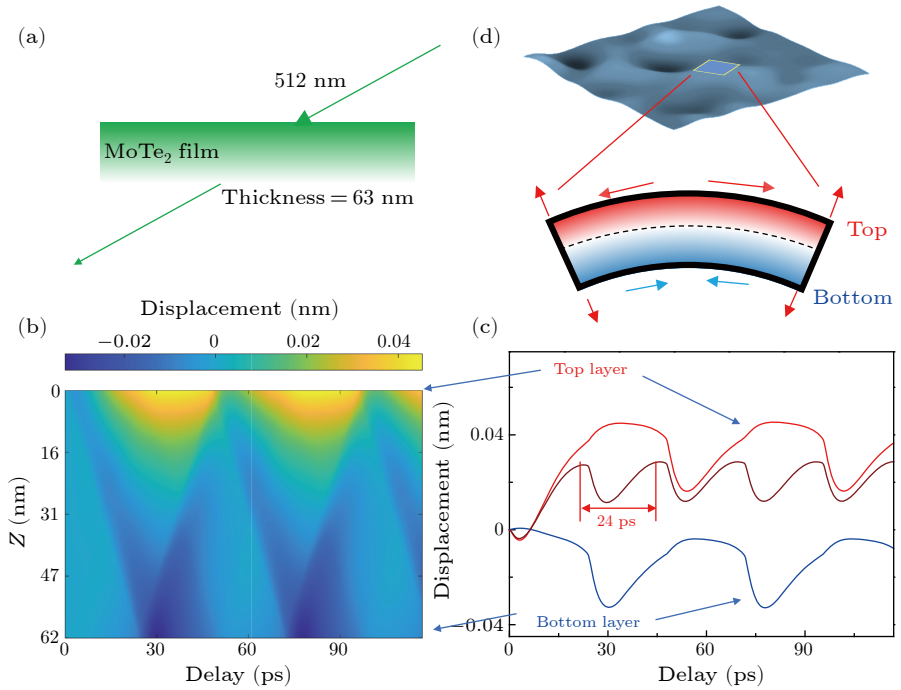

Fig. 4. Theoretical modeling and analysis of the driving mechanism underlying film bending (a) Schematic of the theoretical simulation for the 63 nm 2H-$MoTe_2$ thin film irradiated by 512 nm pump laser. (b) The calculated depth-dependent atomic displacements along the z direction ([001] direction) in the 2H-$MoTe_2$ film. (c) The displacement asymmetry between the top and bottom layers. The brown curve represents the summation of the red and blue curves. (d) The disparity in expansion rates between top and bottom layers, which generates in-plane compressive stresses.

4. Conclusion. We have investigated the picosecond-scale dynamics of laser-induced bending in 2H-$MoTe_2$ thin films under inhomogeneous excitation using ultrafast electron diffraction. Our findings reveal that the interaction of coherent acoustic phonons, particularly the second harmonic, with the material generates a strain gradient along the *c*-axis. This strain gradient, through the Poisson effect, induces a nonuniform in-plane strain, which serves as the primary driving force for the bending of the film. This work provides fundamental insights into the critical role of high-harmonic phonons in ultrafast strain engineering and wrinkle dynamics, significantly advancing our understanding of inhomogeneous excitation mechanisms. These findings open transformative avenues for quantum material design and advanced functional device applications, particularly in the realms of strain-tunable phenomena.

Acknowledgements. This work was supported by the High-level Talent Research Start-up Project Funding of Henan Academy of Sciences (Project No. 241827012), the National Natural Science Foundation of China (Grant Nos. U22A6005 and 62271450), the National Key Research and Development Program of China (Grant Nos. 2021YFA1301502, 2024YFA1408701, and 2024YFA1408403), and the Synergetic Extreme Condition User Facility (SECUF, https://cstr.cn/31123.02.SECUF).

References

[1] Lukashev P and Sabirianov R F 2010 *Phys. Rev. B* **82** 094417
[2] Harbola V, Crossley S, Hong S S, Lu D, Birkhölzer Y A, Hikita Y, and Hwang H Y 2021 *Nano Lett.* **21** 2470
[3] McLeod A S, Zhang J, Gu M Q, Jin F, Zhang G, Post K W, Zhao X G, Millis A J, Wu W B, Rondinelli J M, Averitt R D, and Basov D N 2020 *Nat. Mater.* **19** 397
[4] Hong S S, Gu M, Verma M, Harbola V, Wang B Y, Lu D, Vailionis A, Hikita Y, Pentcheva R, Rondinelli J M, and Hwang H Y 2020 *Science* **368** 71
[5] Chen X, Fan X, Li L, Zhang N, Niu Z, Guo T, Xu S, Xu H, Wang D, Zhang H, McLeod A S, Luo Z, Lu Q, Millis A J, Basov D N, Liu M, and Zeng C 2020 *Nat. Phys.* **16** 631
[6] Liu K, Liu K, Zhang X, Fang J, Jin F, Wu W, Ma C, and Wang L 2024 *Chin. Phys. Lett.* **41** 117701
[7] Yu G L, He X Y, Shi S B, Qiu Y, Zhu M M, Wang J W, Li Y, Li Y X, Wang J, and Zhou H M 2024 *Chin. Phys. Lett.* **41** 057502
[8] Milovanović S P, Andelković M, Covaci L, and Peeters F M 2020 *Phys. Rev. B* **102** 245427
[9] Du D, Manzo S, Zhang C, Saraswat V, Genser K T, Rabe K M, Voyles P M, Arnold M S, and Kawasaki J K 2021 *Nat. Commun.* **12** 2494
[10] Barwick B, Park H S, Kwon O H, Baskin J S, and Zewail A H 2008 *Science* **322** 1227
[11] Chen W, Zhong H, Bao C, Wang F, Cai X, Yun C, Teng H, Wei Z, and Zhou S 2025 *Chin. Phys. Lett.* **42** 017101
[12] Basov D N, Averitt R D, and Hsieh D 2017 *Nat. Mater.* **16** 1077
[13] de la Torre A, Kennes D M, Claassen M, Gerber S, McIver J W, and Sentef M A 2021 *Rev. Mod. Phys.* **93** 041002
[14] Nakamura A, Shimojima T, and Ishizaka K 2021 *Struct. Dyn.* **8** 024103
[15] Duan S F, Cheng Y, Xia W, Yang Y Y, Xu C Y, Qi F F, Huang C Z, Tang T W, Guo Y F, Luo W D, Qian D, Xiang D, Zhang J, and Zhang W T 2021 *Nature* **595** 239
[16] Su Y, Zong A, Kogar A, Lu D, Hong S S, Freelon B, Rohwer T, Wang B Y, Hwang H Y, and Gedik N 2023 *Nano Lett.* **23** 10772
[17] Jeong T Y, Jin B M, Rhim S H, Debbichi L, Park J, Jang Y D, Lee H R, Chae D H, Lee D, Kim Y H, Jung S, and Yee K J 2016 *Acs Nano* **10** 5560
[18] Soubelet P, Reynoso A A, Fainstein A, Nogajewski K, Potemski M, Faugeras C, and Bruchhausen A E 2019 *Nanoscale* **11** 10446
[19] Huitric G, Rodriguez-Fano M, Gournay L, Godin N, Hervé M, Privault G, Tranchant J, Khaldi Z, Cammarata M, Collet E, Janod E, and Odin C 2022 *Faraday Discuss.* **237** 389
[20] Ungeheuer A, Hassanien A S, Mir M T, Nöding L, Baumert T, and Senftleben A 2022 *J. Phys. Chem. C* **126** 19822
[21] Zhang Y, Sun S, Wang W, Tian H, Li J, Li J, and Yang H 2023 *Phys. Rev. B* **108** 245426
[22] Dawson W G and Bullett D W 1987 *Journal of Physics C-Solid State Physics* **20** 6159
[23] Ruello P and Gusev V E 2015 *Ultrasonics* **56** 21
[24] Babilotte P, Ruello P, Mounier D, Pezeril T, Vaudel G, Edely M, Breteau J M, Gusev V, and Blary K 2010 *Phys. Rev. B* **81** 245207
[25] Young E, Akimov A, Campion R, Kent A, Gusev V J P R B C M, and Physics M 2012 *Phys. Rev. B* **86** 155207
[26] Cremons D R, Plemmons D A, and Flannigan D J 2017 *Struct. Dyn.* **4** 044019
[27] Heydenreich J 2010 *Transmission Electron Microscopy* (Springer New York, NY, 2010).
[28] Zhang Y, Li J, Wang W, Tian H, Gao W, Li J, Sun S, and Yang H 2023 *Struct. Dyn.* **10** 064102
[29] Abdullaev N A 2006 *Phys. Solid. State* **48** 663
[30] Mennel L, Paur M, and Mueller T 2018 *APL Photonics* **4** 034404
[31] Zhou Y, Meng Y, Luo G, Chen B, Zhong D, and Hu Y 2024 *ACS Nano* **18** 19783
[32] Zong A, Zhang Q, Zhou F, Su Y, Hwangbo K, Shen X, Jiang Q, Liu H, Gage T E, Walko D A, Kozina M E, Luo D, Reid A H, Yang J, Park S, Lapidus S H, Chu J-H, Arslan I, Wang X, Xiao D, Xu X, Gedik N, and Wen H 2023 *Nature* **620** 988
[33] Cremons D R, Plemmons D A, and Flannigan D J 2016 *Nat. Commun.* **7** 11230
[34] Gnabasik R A, Suri P K, Chen J, and Flannigan D J 2022 *Phys. Rev. Mater.* **6** 024802